

# Estimating the Migrating Diurnal Tide Component of Mesospheric Water Vapor

Cornelius Csar Jude H. Salinas<sup>1,2</sup>, Loren C. Chang<sup>1,2</sup>, Jia Yue<sup>3,4</sup>, Liying Qian<sup>5</sup>, Quan Gan<sup>6</sup>,

James Russell III<sup>7</sup> and Martin Mlynczak<sup>8</sup>

<sup>1</sup>*Department of Space Science and Engineering, National Central University, Zhongli District,*

*Taoyuan City, Taiwan*

<sup>2</sup>*Center for Astronautical Physics and Engineering, National Central University, Zhongli*

*District, Taoyuan City, Taiwan*

<sup>3</sup>*NASA Goddard Space Flight Center, Greenbelt, Maryland, USA*

<sup>4</sup>*Catholic University of America, Washington DC, USA*

<sup>5</sup>*NCAR High Altitude Observatory, Boulder, Colorado, USA*

<sup>6</sup>*Laboratory of Atmospheric and Space Physics, University of Colorado, Boulder, Colorado,*

*USA*

<sup>7</sup>*Hampton University, Hampton, Virginia, USA*

<sup>8</sup>*NASA Langley Research Center, Hampton, Virginia, USA*

Corresponding author: Loren C. Chang, Department of Space Science and Engineering, National  
Central University, Zhongli District, Taoyuan City, Taiwan (loren@g.ncu.edu.tw)

## Abstract

This work presents a method for estimating the migrating diurnal tide (DW1) component of mesospheric H<sub>2</sub>O from observations of the temperature tide and zonal-mean H<sub>2</sub>O made by the Sounding of the Atmosphere using Broadband Emission Radiometry (SABER) instrument. This

work first shows that a 2D least-squares fit on SABER H<sub>2</sub>O yields an erroneous DW1 due to retrieval algorithm problems. Consequently, the adiabatic displacement method is used. Applying the method to SABER observations and comparing with Microwave Limb Sounder (MLS) H<sub>2</sub>O observations reveals that the method reproduces the MLS-observed H<sub>2</sub>O DW1 component best in March and June over low-latitudes in the altitude range between 65 and 75 km where errors range between +5% and +20%. Applying the method for simulations using the Specified Dynamics – Whole Atmosphere Community Climate Model with Ionosphere/Thermosphere eXtension (SD-WACCM-X) indicates that in the model, it is best only in March and not in June. Model simulations further showed that in March, theoretical errors due to the vertical advection assumption and aliasing are best at less than +13% for the low-latitudes and altitudes between 65 km and 75 km. These results therefore lead to the conclusion that despite the errors in the vertical advection assumption and aliasing, the adiabatic displacement method performs best in estimating mesospheric H<sub>2</sub>O DW1 with SABER observations during both March equinox and June solstice over the low latitudes between 65 km and 75 km. Results also show that SD-WACCM-X satisfactorily simulates the H<sub>2</sub>O DW1 magnitude and mechanisms only in the March equinox period.

Index Terms/ Keywords: H<sub>2</sub>O, Tides, Mesosphere

Key Points:

- The adiabatic displacement method estimates mesospheric water vapor's migrating diurnal tide component.
- Estimated mesospheric H<sub>2</sub>O DW1 agrees best with Microwave Limb Sounder observations over the low-latitudes in March and in June.

- Mesospheric H<sub>2</sub>O DW1 is primarily driven by vertical advection in March and June over the low-latitudes.

## 1. Introduction

Water vapor (H<sub>2</sub>O) is a key dynamical tracer in the mesosphere between 60 km and 80 km because its chemical lifetime in this region is around a month (Brasseur and Solomon, 2005). Previous studies have shown, for example, that the mesospheric residual circulation drives zonal-mean H<sub>2</sub>O. Higher zonal-mean H<sub>2</sub>O mixing ratios in the summer mesosphere are driven by the residual circulation's upwelling branch while lower zonal-mean H<sub>2</sub>O in the winter mesosphere is due to the downwelling branch (Dunkerton, 1978; Garcia, 1989; Smith and Brasseur, 1991; Nedoluha et al, 1996; Chandra et al, 1997; Summers et al, 1997; Hervig and Siskind, 2006; Remsberg et al, 2018; Rong et al, 2019). These studies also showed that residual circulation anomalies due to a sudden stratospheric warming can induce enhanced downward transport of zonal-mean H<sub>2</sub>O (Manney et al, 2009; Orsolini et al, 2010; Lee et al, 2011).

While numerous studies have used H<sub>2</sub>O observations to analyze mesospheric zonal-mean dynamics, no work has analyzed mesospheric tides using H<sub>2</sub>O observations. The most dominant atmospheric tide in the mesosphere is the migrating diurnal wave one (DW1) tide which is generated by heating due to lower atmospheric water vapor and ozone. These tides then vertically propagate to the mesosphere and lower thermosphere (MLT) where their amplitudes peak and their dynamical motions affect the ionosphere and thermosphere (Hagan and Forbes, 2002; 2003). DW1 is strongest over the low-latitudes especially during equinox seasons (McLandress, 1997; Zhang et al, 2006; Mukhtarov et al, 2009; Gan et al., 2014). One of the main issues regarding DW1 is our inadequate ability to observe DW1-induced advection and diffusion in the mesosphere. This is because there are minimal satellite-based observations of winds in the region. One way to get

around this is to use dynamical tracers like H<sub>2</sub>O. Hence, understanding how DW1 affects H<sub>2</sub>O allows us to better understand these DW1-induced dynamical motions.

The lack of satellite-based observations attaining full local-time coverage in only a few months has hindered the analysis of tidal impacts on H<sub>2</sub>O. The Microwave Limb Sounder (MLS) onboard the Aura satellite as well as the Michelson Interferometer for Passive Atmospheric Sounding (MIPAS) onboard the Envisat satellite only observe H<sub>2</sub>O over two local-times (Waters et al, 2006; Lambert et al, 2007; Wetzel et al, 2013; Engel et al, 2016). The Atmospheric Chemistry Experiment – Fourier Transform Spectrometer (ACE-FTS) onboard SCISAT-1 also observes H<sub>2</sub>O but it takes almost a year to attain full local-time coverage (Bernath et al, 2005; Carleer et al, 2008). The Solar Occultation for Ice Experiment (SOFIE) onboard the Aeronomy of Ice in the Mesosphere (AIM) satellite also observes H<sub>2</sub>O but only during sunrise and sunset over the mid to high latitudes. (Raspollini et al, 2006; Gordley et al, 2009).

Most recently, new H<sub>2</sub>O profiles were retrieved from infrared limb radiances observed by the Sounding of the Atmosphere using Broadband Emission Radiometry (SABER) instrument onboard the Thermosphere Ionosphere Mesosphere Energetics and Dynamics (TIMED) Satellite (Rong et al, 2019). However for purposes of analyzing the mesospheric tide, only the zonal-mean H<sub>2</sub>O component derived from these H<sub>2</sub>O profiles is valid. This is because it was found that O<sub>3</sub> spectral leakage in the wings of the spectral band causes radiance biases in the H<sub>2</sub>O channel. Rong et al (2019) indicated that the retrieval algorithm empirically removes this leakage by incorporating a single correction coefficient derived in a study using MLS Aura H<sub>2</sub>O data collected at two local times. However, there is no way to empirically remove the local-time dependence of this leakage because there is no independent dataset capable of providing H<sub>2</sub>O profiles with full local-time coverage. Hence, any O<sub>3</sub> local time or tidal variation component still appears in the retrieved H<sub>2</sub>O

even after the O<sub>3</sub> correction. Nevertheless, we still take advantage of these measurements to fill the gap of estimating H<sub>2</sub>O's DW1 component in the mesosphere by applying the adiabatic displacement method to SABER observations of the H<sub>2</sub>O zonal-mean component and temperature. This involves testing and quantifying the errors of the method using simulations from the Specified Dynamics – Whole Atmosphere Community Climate Model – eXtended (SD-WACCM-X) v2.1 as shown later. It will also be shown that the presented method provides a way to deduce DW1-induced vertical advection which is currently still notoriously difficult to measure because of the lack of global satellite observations of vertical winds. Because vertical advection is fundamentally important in the vertical coupling of the atmosphere, lack of observations of the processes involved have hindered our full understanding of the process (Jones et al, 2014).

This manuscript is organized as follows. Section 2 presents the SABER observations, MLS observations and SD-WACCM-X simulations. First, problems with simply doing a least-squares fit on SABER H<sub>2</sub>O observations to estimate the mesospheric H<sub>2</sub>O DW1 component are presented. Then, the section presents the adiabatic displacement method. Section 3 shows the application of the method using SABER H<sub>2</sub>O and temperature observations and the results are then compared with MLS H<sub>2</sub>O observations. Section 4 shows the application of the method using SD-WACCM-X outputs. A tendency analysis using SD-WACCM-X is included to further explain the performance of the method. This tendency analysis compares the role of vertical advection with other possible mechanisms. Section 5 presents a calculation of the errors in the estimated mesospheric H<sub>2</sub>O DW1 due to aliasing. The daily zonal-mean profile of mesospheric H<sub>2</sub>O provided by SABER is important when using the adiabatic displacement method. Although SABER has full local-time coverage, the sampling is not as regular in longitude and LT as a model's sampling. An effect of this irregular sampling is that local-time variations may still alias

into the calculated daily zonal-mean profile. Consequently, section 5 calculates the errors due to this aliasing. Finally, section 6 presents the summary and conclusions.

## **2. SABER observations, MLS observations and SD-WACCM-X simulations**

This section presents the SABER observations, the previously described problem with the SABER H<sub>2</sub>O observations, and how we addressed this problem in order to estimate SABER H<sub>2</sub>O DW1. This section will also present the MLS observations as well as the SD-WACCM-X simulations.

This work uses SABER v2.07 operational temperature and H<sub>2</sub>O observations from the SABER instrument onboard the TIMED satellite for the period February 2002 to December 2019 (Russell et al, 1999). SABER v2.07 operational temperature profiles are retrieved from the 15  $\mu$ m CO<sub>2</sub> channel with the assumption of no local-time variation in CO<sub>2</sub> (Mertens et al, 2001; Kutepov et al, 2006; Garcia-Comas et al, 2008; Mertens et al, 2009; Dawkins et al, 2018). Salinas et al (2020) has pointed out that the assumption of no local-time variation in CO<sub>2</sub> may be problematic above 90 km, however, this work focuses on altitudes below 80 km where the CO<sub>2</sub> vertical gradient and thus local-time variations are negligible (Garcia et al, 2014; Salinas et al, 2020). SABER v2.07 H<sub>2</sub>O volume mixing ratio (VMR) vertical profiles are retrieved from the instrument's 6.8  $\mu$ m channel which are valid between ~16 km and ~83 km although at around 80 km, errors reach up to ~30% (Rong et al, 2019). These are the first satellite-based observations of H<sub>2</sub>O that provide full local-time coverage after 60 days of observations [See figure 3 of Rong et al (2019)].

This work also uses simulations from the Specified Dynamics – Whole Atmosphere Community Climate Model – eXtended (SD-WACCM-X) v2.1. WACCM-X is a first-principles physics-based model that simulates the whole atmosphere from the surface to the

134 Ionosphere/Thermosphere up to around 700 km depending on solar activity while accounting for  
135 the coupling of the atmosphere with the ocean, sea ice and land. It uses elements of both the Whole  
136 Atmosphere Community Climate Model and the Thermosphere Ionosphere electrodynamics  
137 general circulation models (Liu, H.L. et al, 2018; Liu, J., et al, 2018). Liu et al (2018) has compared  
138 temperature DW1 in this model with SABER temperature DW1 and they showed that it is  
139 substantially improved. SD-WACCM-X is a version of WACCM-X that is nudged by the Modern-  
140 Era Retrospective Analysis for Research and Applications (MERRA) Reanalysis dataset  
141 (*Rienecker et al*, 2011; *Marsh et al*, 2013). In brief, nudging relaxes the model neutral winds and  
142 temperatures below ~50 km towards MERRA reanalysis values. Thus, these model parameters  
143 become realistic from the surface to the stratosphere. For more information on this method of  
144 constraining the model with reanalysis data, see Kunz et al (2011). The model was run from 2000  
145 to 2019 with a horizontal resolution of 1.9° in latitude and 2.5° in longitude but we only use data  
146 from 2002 to 2019 to match that of SABER observations. The vertical resolution is 2 points per  
147 scale height below ~50 km and increases to 4 points per scale height above ~50 km. Bi-monthly  
148 means of variables such as winds, temperature, geopotential height and eddy diffusion as well as  
149 water vapor were calculated from these simulations. When calculating the bi-monthly means, the  
150 center of the averaging window is on the 15<sup>th</sup> of each month. For example, when this paper  
151 mentions temperature in March, this refers to the use of profiles retrieved within +/-30 days of the  
152 15<sup>th</sup> of March between 2002 and 2019. From these bi-monthly means, a seasonal climatology using  
153 all data from 2002 to 2019 was calculated. This will cancel out interannual phenomena that are  
154 known to affect DW1 such as the quasi-biennial oscillation (Pancheva et al, 2009).

When a dataset attains full local-time coverage, as is the case for SABER H<sub>2</sub>O, 2D least-squares fit can be used to calculate the DW1 amplitudes and phases. The fit uses basis functions of the following form (Wu et al, 1995):

$$\mu(\lambda, t) = \bar{\mu} + \sum_{n=1}^3 \sum_{s=-4}^4 \hat{\mu}_{n,s} \cos(n\Omega t - s\lambda - \hat{\psi}_{n,s}) + \sum_{s=1}^4 \hat{\mu}_s \cos(s\lambda - \hat{\psi}_s) \quad (1)$$

In this equation,  $\mu$  is the VMR of H<sub>2</sub>O (in parts-per-million-volume).  $\bar{\mu}$  is the zonal-mean VMR of H<sub>2</sub>O. The second summation term comprises of the migrating and non-migrating diurnal ( $n = 1$ ), semidiurnal ( $n = 2$ ) and terdiurnal ( $n = 3$ ) tides with wavenumbers ( $s$ ) from -4 to 4. The third summation term includes the stationary planetary waves with wavenumbers from 1 to 4. The quantities  $\hat{\mu}$  and  $\hat{\psi}$  are the amplitudes and phases, respectively.

To calculate the DW1 component from SABER H<sub>2</sub>O or temperature profiles, profiles were collected into a non-overlapping 5-degree latitude bin from latitude 90S to 90N over a bi-monthly window centered on the 15<sup>th</sup> day of every month. Bi-monthly or around 60 days of SABER profiles is needed because it takes 60 days for SABER to attain full local-time coverage. Finally, at each latitude-altitude grid point, a 2D least-squares fit was used to calculate the DW1 amplitude and phases. To calculate the DW1 component from SD-WACCM-X simulations, a 2D least-squares fit was also applied.

Figure 1.A and 1.B shows the DW1 amplitude and phases of SABER H<sub>2</sub>O for March equinox averaged for all years of observations, respectively, as a function of latitude and altitude. Comparing with model simulations in figure 1.C and 1.D, the DW1 amplitude of this original SABER H<sub>2</sub>O exhibits a primary equatorial peak but its amplitude is almost three times larger than simulations. The mid-latitude peaks of SABER H<sub>2</sub>O's DW1 component are also different from simulations. The simulations show clear secondary mid-latitude peaks for latitudes greater than 35



degrees and altitudes greater than 75 km. SABER H<sub>2</sub>O's DW1 amplitude in March shows one secondary peak southward of 30 degrees below 75 km.

As for the phase, the DW1 phase of SD-WACCM-X H<sub>2</sub>O in figure 1.D exhibits features consistent with a vertically propagating mode. The DW1 phase of this original SABER H<sub>2</sub>O exhibits minimal phase variation with altitude. If one solely considers atmospheric physics and chemistry, these features would seem to suggest unexpected dynamical and/or chemical mechanisms controlling mesospheric H<sub>2</sub>O. However, it is now suspected that these features may be a result of retrieval algorithm problems. As mentioned earlier, O<sub>3</sub> spectral leakage causes any O<sub>3</sub> local time or tidal variation component to also appear in the retrieved H<sub>2</sub>O. This is exacerbated by the significant local-time variations in mesospheric O<sub>3</sub> (Smith et al, 2011b; Smith et al, 2013). These results indicate that a 2D least-squares fit applied in the data yields an inaccurate SABER H<sub>2</sub>O DW1.

Rong et al (2019) presents the complete process describing how the effect on SABER retrieved H<sub>2</sub>O of spectral out-of-band (OOB) O<sub>3</sub> emission in the wings of the H<sub>2</sub>O filter is removed. In brief, the process involves using MLS Aura H<sub>2</sub>O daily zonal-mean profiles to empirically determine a single SABER out-of-band (OOB) radiance correction coefficient. Because of SABER's precession, 60-days of SABER H<sub>2</sub>O observations are required to calculate the daily-mean zonal-mean SABER H<sub>2</sub>O. With this sampling, a daily zonal-mean H<sub>2</sub>O dataset is required to minimize the OOB errors on the daily- zonal-mean SABER H<sub>2</sub>O component. MLS measures H<sub>2</sub>O globally every day at two local-times that are 12 hours apart; one at ~01:45 AM and another at ~1:45 PM. With this sampling, daily zonal-mean MLS H<sub>2</sub>O with minimal diurnal tidal aliasing can be calculated. Thus, the correction uses this dataset. In short, this correction was designed to remove the O<sub>3</sub> contamination of SABER H<sub>2</sub>O radiances for the daily zonal

mean only. Local time variation of O<sub>3</sub> OOB is not corrected at all. This has allowed studies (Yue et al, 2019; Yu et al, 2022) to already use SABER H<sub>2</sub>O to analyze the zonal-mean component of mesospheric H<sub>2</sub>O. However, this correction will only perfectly work if the daily zonal-mean profile was calculated using a sampling pattern the same as that in a model; that is, full local-time coverage in a day with a regular longitude-UT sampling. SABER requires 60 days to achieve full local-time coverage and the longitude-UT sampling is irregular. Hence, aliasing is expected. Here, we quantify the alias on the zonal-mean due to the erroneous SABER H<sub>2</sub>O DW1. This will later be used to quantify the errors of our method in estimating SABER H<sub>2</sub>O DW1.

To calculate the alias on the zonal-mean due to DW1, SABER H<sub>2</sub>O profiles were first collected into non-overlapping 5-degree latitude bin from latitude 90S to 90N over a bi-monthly window centered on the 15<sup>th</sup> day of every month. A 2D least-squares fit is then used to get the amplitudes and phases of SABER H<sub>2</sub>O DW1. However, apart from applying 2D least-squares fits on these profiles, we also get the longitude and UT information of all the profiles in these bins. This information is used to synthesize a cosine signal expressed as:

$$N(\lambda, t) = \hat{N} \cos\left(\frac{2\pi t_{UT}}{24} - \lambda - \phi_N\right) \quad (2)$$

Here,  $\hat{N}$  and  $\phi_N$  are the amplitudes and phases of the erroneous SABER H<sub>2</sub>O DW1. Finally, all the synthesized profiles at each altitude-latitude bin are averaged. This process is adapted from Wu et al (2005). This yields the alias on the zonal-mean due to the problematic SABER H<sub>2</sub>O DW1 and also a latitude-pressure profile of alias values. Figure 1.E shows such a profile when this process is applied to 60 days of SABER H<sub>2</sub>O profiles centered on March 15 of 2005. Figure 1.E shows that regions where the erroneous SABER H<sub>2</sub>O DW1 attain peak amplitudes correspond to an error of around -0.3 ppm in the estimated zonal-mean component. The average error in this

region is around -0.1 ppm. Considering the values of zonal-mean H<sub>2</sub>O in this region range between 3 to 7 ppm, zonal-mean errors due to alias are consistently less than 5%.

The problem with the SABER H<sub>2</sub>O dataset clearly requires a different approach to estimate SABER H<sub>2</sub>O DW1. The estimation technique used in this study is the adiabatic displacement method (Eckermann et al, 1998). It assumes that the DW1 component of H<sub>2</sub>O is predominantly driven by DW1-induced vertical advection. Previous studies used the same approach in analyzing tidal variations of atomic oxygen and NO in the mesosphere and lower thermosphere (Ward et al, 1999; Marsh and Russell, 2000; Oberheide et al, 2003; Oberheide and Forbes, 2008; Smith et al 2010). Yue and Gan (2021) recently applied this method to determine the quasi-2-day wave modulations of mesospheric CO<sub>2</sub>. An important advantage of this method is that to quantify wave-induced perturbations in constituents, this approach only requires observations of temperature and the zonal mean distribution of chemical tracers. To estimate vertical advection, we first reduce the linearized continuity equation to only account for vertical wind and then evaluate it by setting all primed variables into the form  $e^{i(kx-\sigma t)}$  where  $k$  is the zonal wave number and  $\sigma$  is the tidal frequency. This yields:

$$i(k\bar{u} - \sigma)\mu' + \frac{\partial \bar{\mu}}{\partial z}w' = 0 \quad (3)$$

For this and the rest of the equations shown in this paper, variables with an overbar denote zonal-means while primed variables denote tidal perturbations.  $\mu$  is H<sub>2</sub>O volume mixing ratio,  $z$  is geopotential height.  $w$  is the vertical wind. The same can be done to a form of the thermodynamic equation that assumes all temperature changes are due to adiabatic motion. This yields:

$$i(k\bar{u} - \sigma)T' + Sw' = 0 \quad (4)$$

243 where  $S = \left( \frac{\partial T}{\partial z} + \frac{g}{c_p} \right)$  is static stability,  $g$  is the acceleration due to gravity ( $9.8 \text{ m/s}^2$ ) and  $c_p$  is  
 244 the heat capacity of air at constant pressure ( $1004 \text{ J K}^{-1} \text{ kg}$ ).  $u$  is zonal wind.  $T$  is temperature.  
 245 Combining equations 3 and 4 gives us:

$$246 \quad \mu' = \frac{T'}{S} \frac{\partial \bar{\mu}}{\partial z} \quad (5)$$

247 This equation gives the perturbation of the tracer  $\mu'$  due to vertical advection as expressed on the  
 248 right-hand-side.

249 To validate the estimated DW1 component of H<sub>2</sub>O from SABER observations, we use Aura  
 250 MLS H<sub>2</sub>O VMR version 4.2x (V4.2x) data (Lambert et al., 2007) from 2004 to 2019. Typical  
 251 precisions of the MLS H<sub>2</sub>O are 0.3–2 ppmv over the pressure range of 68 to 0.002 hPa. Vertical  
 252 resolutions are 3–4 km at pressures >2 hPa, 5–7km at 1–0.2 hPa, and 12–16 km at pressures <0.1  
 253 hPa (Lambert et al., 2007). MLS observes H<sub>2</sub>O globally at ~1:45AM (hereafter mentioned as  
 254 ~2AM) and ~1:45PM (hereafter mentioned as ~2PM) local-time. From these observations, one  
 255 can construct monthly-mean ~2AM and ~2PM zonal profiles of H<sub>2</sub>O. Taking the differences of  
 256 these profiles then give an estimate of the DW1-induced perturbations on H<sub>2</sub>O.

### 257 **3. Results: Application of the technique to SABER observations**

258 In this section, we apply the adiabatic displacement method to SABER H<sub>2</sub>O and  
 259 temperatures observations. We then validate the method by comparing the estimated SABER H<sub>2</sub>O  
 260 DW1 with MLS H<sub>2</sub>O DW1. Figure 2 shows an application of the method for March equinox. This  
 261 figure shows the main parameters required for the adiabatic displacement method. Figure 2.A  
 262 shows the zonal-mean profile of SABER H<sub>2</sub>O between 65 km and 80 km over latitudes 50S to  
 263 50N. It shows that SABER H<sub>2</sub>O's zonal-mean values are higher over the southern hemisphere than

264 over the northern hemisphere. Previous studies have shown that this is due to the residual  
265 circulation (Dunkerton, 1978; Garcia, 1989; Smith and Brasseur, 1991; Nedoluha et al, 1996;  
266 Chandra et al, 1997; Summers et al, 1997; Hervig and Siskind, 2006; Remsberg et al, 2018; Rong  
267 et al, 2019). Figure 2.B shows the vertical gradient of zonal-mean SABER H<sub>2</sub>O. The gradient is  
268 negative throughout the mesosphere with the largest gradients found above 70 km. This is due to  
269 the effects of photodissociation (Brasseur and Solomon, 2006). Figure 2.C shows the DW1  
270 amplitudes of SABER temperature. SABER temperature DW1 has primary peak amplitudes of  
271 around 10K over the low latitudes above 75 km and secondary peak amplitudes of around 7K over  
272 the northern mid-latitudes. There is also a local maximum over the southern low-latitudes with  
273 amplitudes of around 3K. Figure 2.D shows the DW1 amplitudes of SABER H<sub>2</sub>O calculated using  
274 the adiabatic displacement method (SABER advected H<sub>2</sub>O DW1 hereafter) in March as a function  
275 of latitude and altitude. For all latitudes, the highest amplitudes are found above 70 km. Results  
276 show a peak amplitude of around 0.5 ppm over the equator. There is a secondary maximum of  
277 around 0.2 ppm over latitude 50N. To validate SABER advected H<sub>2</sub>O DW1, we compared them  
278 with the DW1 amplitudes estimated from MLS H<sub>2</sub>O. MLS measures H<sub>2</sub>O along daily ascending  
279 and descending orbits. The ascending (descending) nodes of the Aura orbit provide MLS H<sub>2</sub>O  
280 observations at around 2PM (2AM) local-time. This provides us with daily zonal-mean profiles of  
281 H<sub>2</sub>O at two local times that are 12-hour apart. Taking the differences of these zonal-mean profiles  
282 gives an estimate of the perturbations of DW1 on H<sub>2</sub>O. To get the differences at 2 AM and at 2  
283 PM with SABER, we first reconstructed SABER H<sub>2</sub>O at these local-times by using the SABER  
284 advected H<sub>2</sub>O DW1 amplitudes and phases. Then, we calculated their differences. Figure 2.E  
285 shows the differences between SABER advected H<sub>2</sub>O DW1 H<sub>2</sub>O at 2AM and SABER advected  
286 H<sub>2</sub>O DW1 at 2PM for March equinox. From this perspective, there is a peak positive anomaly of

around 0.6 ppm between altitudes 70 km and 80 km over latitudes 10S and 10N. There is also a peak negative anomaly of around -0.3 ppm between altitudes 70 km and 80 km over the southern mid-latitudes. Figure 2.F shows the differences between MLS H<sub>2</sub>O at 2AM and MLS H<sub>2</sub>O at 2PM for March equinox. MLS also observes a peak positive anomaly of around 0.5 ppm between altitudes 70 km and 80 km over latitudes 10S and 10N. Over the low-latitudes, the differences range between +5% to +20% with the location of the +20% error found over the region where the 2AM-2PM difference of SABER advected H<sub>2</sub>O DW1 reaches +0.6 ppm. MLS also observes a peak negative anomaly of around -0.6 ppm between altitudes 70 km and 80 km over the southern mid-latitudes. However, SABER advected H<sub>2</sub>O DW1 does not satisfactorily capture the overall latitudinal structure observed by MLS above 65 km. The most notable differences in the latitude structure are found over the mid-latitudes.

Figure 3 shows an application of the method for June solstice and it is formatted in a similar way to figure 2. Figures 3.E and 3.F clearly show that in June solstice, the best agreement between SABER advected H<sub>2</sub>O DW1 and MLS H<sub>2</sub>O DW1 is over the low-latitudes where there is a region of peak positive anomaly. Their values are both around +0.2 ppm and their overall spatial pattern is similar. Figure 2 and 3 clearly indicate that for both seasons, the method performs best over the low-latitudes.

#### **4. Results: Application of the technique to SD-WACCM-X**

In this section, we apply the method on model outputs. With the self-consistency of the model compared to a comparison between two satellite platforms in SABER and MLS, we are able to give a theoretical approximation of the errors of the adiabatic displacement method. In particular, we quantify the error due to the assumption of vertical advection's predominance. We

then determine if the method yields results consistent with a tendency analysis of the continuity equation. We also use the tendency analysis to further explain the method's performance.

Figure 4 shows an application of the method for March equinox. We only present model results in latitudes between 50S and 50N for consistency with SABER observations' latitudinal coverage. We also present model H<sub>2</sub>O up to 80 km because this is also the highest altitude where SABER H<sub>2</sub>O is reliable. Figure 4.A shows the zonal-mean profile of SD-WACCM-X H<sub>2</sub>O. Comparison of figures 2.A and 4.A shows that the zonal-mean component of SABER H<sub>2</sub>O and SD-WACCM-X H<sub>2</sub>O have clear differences in their magnitudes. Between 70 km and 80 km, the SD-WACCM-X H<sub>2</sub>O zonal-mean has lowest values of around 2.5 ppm while SABER's lowest values are only 4 ppm. Figure 4.B shows the vertical gradient of SABER H<sub>2</sub>O zonal-mean for March equinox. Comparison of figure 2.B and 4.B shows that the vertical gradients of the zonal-mean component of SABER H<sub>2</sub>O and SD-WACCM-X H<sub>2</sub>O also have clear differences. The gradients above 70 km are larger in SD-WACCM-X than in SABER H<sub>2</sub>O. Figure 4.C shows the DW1 component of SD-WACCM-X temperatures for March equinox. The primary peak over the low-latitudes in SD-WACCM-X temperature DW1 has similar amplitudes to that of SABER temperature DW1. On the other hand, SD-WACCM-X temperature DW1 exhibits a latitudinal structure more consistent with the (1,1) mode. The secondary mid-latitude peaks in SD-WACCM-X temperature DW1 also exhibit an asymmetry in their amplitudes but the location of the northern mid-latitude peak is more equatorward than in SABER temperature DW1. Its magnitude is also weaker. These differences could indicate that the model's H<sub>2</sub>O photochemistry, residual circulation or gravity wave parameterizations may not be realistic. Figure 4.D shows the DW1 component of SD-WACCM-X calculated using the adiabatic displacement method (hereafter referred to as SD-WACCM-X advected H<sub>2</sub>O DW1). Figure 4.E shows the percent differences

between SD-WACCM-X H<sub>2</sub>O DW1 (in figure 1.C) and SD-WACCM-X advected H<sub>2</sub>O DW1. Positive percent differences indicate SD-WACCM-X advected H<sub>2</sub>O DW1 is larger than SD-WACCM-X H<sub>2</sub>O DW1. The lowest percent differences are over the low-latitudes between 65 km and 75 km with values ranging from +2% to +8%. Figures 2 and 4 indicates that for both SABER and SD-WACCM-X, the method performs best over the low-latitudes during March equinox.

Figure 5 shows an application of the method for June solstice and it is formatted in a similar way to figure 4 but with the addition of figure 5.D which shows the DW1 component of SD-WACCM-X H<sub>2</sub>O in June solstice calculated using 2D least-squares fit. Figure 5.F indicates that there are minimal areas with percent differences less than 10%. Over the low-latitudes, percent differences range between +20 to +40% between 60 km and 70 km while they range between -15 to -30% between 70 km and 80 km. Figures 3 and 5 indicates that for SABER and SD-WACCM-X, the method performs best over the low-latitudes during June solstice. However, the method performs better by almost 10% with SABER than with SD-WACCM-X during June solstice. This could indicate that in June solstice, the role of vertical advection in SD-WACCM-X H<sub>2</sub>O DW1 may have significant inaccuracies.

We now assess whether this method is consistent with the results of a tendency analysis involving the continuity equation. A tendency analysis more accurately determines the importance of vertical advection in the DW1 component of a tracer because it involves comparing the importance of vertical advection with the other possible mechanisms. Since we are analyzing tides, we utilize a linearized version of the continuity equation:

$$\left(\frac{\partial}{\partial t} + \frac{\bar{u}}{a \cos \phi} \frac{\partial}{\partial \lambda}\right) \mu' + \left(\frac{v'}{a}\right) \frac{\partial \bar{\mu}}{\partial \phi} + w' \frac{\partial \bar{\mu}}{\partial z} - \frac{1}{\rho_0} \frac{\partial}{\partial z} \left(\rho_0 K_{zz}' \frac{\partial \bar{\mu}}{\partial z}\right) - \frac{1}{\rho_0} \frac{\partial}{\partial z} \left(\rho_0 D_{\mu}' \frac{\partial \bar{\mu}}{\partial z}\right) = -L_1' \bar{\mu} - L_2' \bar{\mu} - L_3' \bar{\mu}$$

(6)



354  $L_1$ ,  $L_2$  and  $L_3$  are photochemical loss rates for chemical equations 7, 8 and 9 shown below,  
 355 respectively. These reactions are driven by Lyman-alpha (Lyman- $\alpha$ ) and are the main reactions  
 356 controlling mesospheric H<sub>2</sub>O (Brasseur and Solomon, 2006). Equation 7 involves the production  
 357 of hydrogen  $H$  and hydroxyl  $OH$  radicals. It is given by:



359 Equation 8 involves the production of molecular hydrogen  $H_2$  and atomic oxygen in an excited  
 360 singlet state  $O(^1D)$ . It is given by:



362 Equation 9 involves the production of two hydrogen atoms and atomic oxygen  $O$ . It is given by:



364  $t$  is time,  $\phi$  is latitude,  $\lambda$  is longitude and  $z$  is geopotential height. The variables  $u$ ,  $v$  and  $w$  are the  
 365 neutral zonal, meridional and vertical winds, respectively;  $K_{zz}$  is the eddy diffusion coefficient;  $D_\mu$   
 366 is the molecular diffusion coefficient;  $\rho_0$  is the atmospheric neutral density; and  $a$  is the radius of  
 367 the Earth which is  $6.37 \times 10^6$  m. Note that the eddy diffusion coefficient is calculated from a  
 368 gravity wave parameterization (Richter et al, 2010; Garcia et al, 2017). The molecular diffusion  
 369 coefficient is as defined in Smith et al (2011a). Equation 9 states that H<sub>2</sub>O's tidal perturbations are  
 370 controlled by the tidal perturbations in winds, diffusion and local-time variations in photochemical  
 371 loss reactions as well as meridional or vertical gradients of H<sub>2</sub>O. To determine the contribution of  
 372 each wind-field, diffusion coefficients and photochemical loss reactions, we calculate each term  
 373 in equation 9 and then calculate their DW1 amplitudes and phases. However, we will only show  
 374 the DW1 amplitudes of these terms because this is enough to indicate that a given process is  
 375 dominant. A similar approach has been applied to other tracers (Akmaev and Shved, 1980;

Shepherd et al, 1995; Shepherd et al, 1997; Angelats i Coll and Forbes, 1998; Zhang et al, 1998; Ward, 1998; Marsh et al, 1999; Ward, 1999; Wu et al, 2003; Smith et al, 2010; Salinas et al, 2020).

Figure 6.A to 6.F shows the March equinox amplitudes of the DW1 component of all the terms in equation 2 as a function of latitude and altitude. The tendencies due to all three photochemical loss reactions are first combined and their DW1 component's amplitude shown in figure 4.D. Figure 4.A shows the amplitudes of the DW1 amplitude of the time-rate-of-change of H<sub>2</sub>O VMR ( $(\frac{\partial}{\partial t} + \frac{\bar{u}}{a \cos \phi})\mu'$ ) as defined in equation 2. This is the first term in equation 2. Peak DW1 amplitudes of  $(\frac{\partial}{\partial t} + \frac{\bar{u}}{a \cos \phi})\mu'$  are around 2.5 ppm/day and are found over the low-latitudes above 70 km. Secondary peaks with values of around 1 ppm/day are found over the mid-latitudes above 75 km. Our tendency analysis will determine now how much the other terms in equation 4 contribute to this first term. Figures 6.B to 6.F show that the vertical advection tendency ( $w'\frac{\partial \bar{\mu}}{\partial z}$ ) in figure 6.B has the highest amplitudes. The vertical advection peak has primary peak DW1 amplitudes over the low-latitude and secondary peaks over the mid-latitudes, which is similar with the DW1 component of  $(\frac{\partial}{\partial t} + \frac{\bar{u}}{a \cos \phi})\mu'$ . However, the vertical advection tendency's equatorial peak extends from 65 km to 80 km while the equatorial peak of  $(\frac{\partial}{\partial t} + \frac{\bar{u}}{a \cos \phi})\mu'$  only extends between 65 km and 75 km. Also, the vertical advection tendency's secondary mid-latitude peaks are weaker than that of  $(\frac{\partial}{\partial t} + \frac{\bar{u}}{a \cos \phi})\mu'$ . Over mid-latitudes, photochemistry and meridional advection's DW1 amplitudes are comparable to vertical advection suggesting that these three mechanisms are very important. Over the low-latitudes, photochemistry has the second highest amplitudes. This indicates that to fully reproduce the DW1 amplitudes above 75 km over the equator, photochemistry is also needed. Figure 6.E and 6.F show that eddy and molecular diffusion

play a negligible role in H<sub>2</sub>O's DW1 component. These indicate that in SD-WACCM-X, the DW1 component of H<sub>2</sub>O is primarily driven by vertical advection with secondary contributions from meridional advection and photochemistry. Figure 4 and figure 6 show that the region where SD-WACCM-X advected H<sub>2</sub>O DW1 and SD-WACCM-X H<sub>2</sub>O DW1 have percent differences less than 8% is also the same region where SD-WACCM-X H<sub>2</sub>O DW1 is primarily driven by vertical advection. Figure 4 and figure 6 also show that regions with percent differences greater than 10% are also regions where meridional advection and photochemistry are no longer negligible. Figure 4 and figure 6 show that the adiabatic displacement method is consistent with the results of a tendency analysis.

Figure 7.A to 7.F shows the same as figure 6A. to 6.F but for June solstice. Peak DW1 amplitudes of  $\left(\frac{\partial}{\partial t} + \frac{\bar{u}}{a \cos \phi}\right)\mu'$  in June solstice are around 1.5 ppm/day and are found over the northern high-latitudes above 75 km. Over the low-latitudes, peak amplitudes are around 0.8 ppm/day between 70 and 80 km. Over the northern high-latitudes, it is clear that photochemical loss reactions shown in figure 7.D are most important with secondary contributions from meridional advection in figure 7.C. Over the low-latitudes, both vertical advection in figure 7.B and photochemical loss reactions have comparable magnitudes. Figure 7 indicates that the poor performance of the method in June solstice for all latitudes and altitudes, as shown in figure 5, is due to the non-negligible importance of both meridional advection and photochemical loss reactions for all latitudes and altitudes. Since the method performs better with observations, our results indicate that the non-negligible importance of both meridional advection and photochemical loss reactions for all latitudes and altitudes in the model may be inaccurate.

## 5. Errors due to Aliasing

Although SABER H<sub>2</sub>O has full local-time coverage, it requires 60 days of observations to attain this. Strictly speaking, this very long window does not fully remove aliasing although it has always been accepted that the amount of aliasing is minimal. For a more thorough analysis, this section quantifies the errors due to aliasing as a result of requiring 60 days of observations to attain full local-time coverage.

To quantify the error due to aliasing, our method involves the use of both SABER H<sub>2</sub>O profiles and SD-WACCM-X H<sub>2</sub>O profiles. Owing to the poor performance of the method with model outputs for June solstice, we only quantify the errors due to aliasing for March equinox. With the SABER H<sub>2</sub>O profiles, we can calculate the alias on the zonal-mean due to the erroneous SABER H<sub>2</sub>O DW1. With the SD-WACCM-X H<sub>2</sub>O profiles, we can calculate a correct zonal-mean H<sub>2</sub>O. Combining both gives us an erroneous zonal-mean H<sub>2</sub>O that we can then use to calculate an erroneous SD-WACCM-X advected H<sub>2</sub>O DW1. We then compare this with the correct SD-WACCM-X H<sub>2</sub>O.

We have already calculated the alias on the zonal-mean due to the erroneous SABER H<sub>2</sub>O DW1 in figure 1.E. Figure 8.A shows the sum of the correct zonal-mean SD-WACCM-X H<sub>2</sub>O and the alias errors in figure 1.E. Figure 8.B shows the percent error on the correct zonal-mean SD-WACCM-X H<sub>2</sub>O due to the alias errors. Figure 8.B shows a spatial pattern similar to that of the erroneous SABER H<sub>2</sub>O DW1 which is expected. Regions of high SABER H<sub>2</sub>O DW1 amplitudes should coincide with regions of high alias values. Over the low-latitudes where our method has already been shown to perform well, the largest errors on the zonal-mean H<sub>2</sub>O are around -6%. This erroneous zonal-mean is then used to calculate an SD-WACCM-X advected DW1 component. Figure 8.C shows this new component. Figure 8.D shows the difference between this erroneous new DW1 component and SD-WACCM-X H<sub>2</sub>O DW1 solely calculated

using a 2D least-squares fit. We can see that over the low-latitudes, the largest errors have now increased to around +13%. This indicates that the aliasing causes a ~5% increase in the errors.

## 6. Summary and Conclusions

This work estimates the DW1 component of mesospheric H<sub>2</sub>O using SABER H<sub>2</sub>O and temperature profiles. We first show that using a 2D least-squares fit on SABER H<sub>2</sub>O profiles yields a DW1 component that is erroneous due to retrieval algorithm problems. Instead therefore, the adiabatic displacement method is used to estimate the DW1 component of mesospheric H<sub>2</sub>O. This method assumes that the DW1 component of H<sub>2</sub>O is predominantly driven by DW1-induced vertical advection. Results show that for March equinox, both SABER advected H<sub>2</sub>O DW1 and MLS H<sub>2</sub>O DW1 exhibit peak positive anomalies of around 0.5 – 0.6 ppm between altitudes 70 km and 80 km over latitudes 10S and 10N. The differences appear to range between +5% to +20% with the location of the +20% error found over the region where the 2AM-2PM difference of SABER advected H<sub>2</sub>O DW1 reaches +0.6 ppm. Both SABER advected H<sub>2</sub>O DW1 and MLS H<sub>2</sub>O DW1 also exhibit a peak negative anomaly between altitudes 70 km and 80 km over the southern mid-latitudes. However, the differences in their values are larger than 20%. For June solstice, the best agreement is also found over the low-latitudes with differences of around 10% to 15%.

We then applied the adiabatic displacement method on SD-WACCM-X model outputs also for March equinox and June solstice. With the self-consistency of the model, we can calculate a theoretical approximation of the errors of the adiabatic displacement method. In particular, we quantify the error due to the assumption of vertical advection predominance. We also did a tendency analysis to further explain the method's behavior especially in terms of the validity of the assumptions. Results show that for March equinox, the method yields the lowest

errors of less than 8% over the low-latitudes between 65 km and 75 km. A tendency analysis revealed that this is indeed a region where vertical advection primarily drives the DW1 component of H<sub>2</sub>O. In other regions, photochemistry or meridional advection are non-negligible. For June solstice, the method yields errors of at least 20% over most of the mesosphere. This clearly disagrees with the SABER and MLS observations. A tendency analysis revealed that in the June solstice period, photochemistry and meridional advection are non-negligible throughout the mesosphere. The disagreement in the method's performance in June solstice between the observations and the model indicate that there may be a problem with the physical mechanisms of SD-WACCM-X H<sub>2</sub>O DW1 in this season.

After quantifying the errors due to the vertical advection assumption, we then quantified the errors due to aliasing. We only do this analysis for March equinox because we have already shown that there is a problem with SD-WACCM-X H<sub>2</sub>O DW1 in June solstice. As mentioned earlier, the DW1 component of SABER H<sub>2</sub>O is erroneous. With SABER's imperfect sampling, this could yield an aliasing into the zonal-mean component of SABER H<sub>2</sub>O. Results of our aliasing analysis indicate that regions with the highest erroneous SABER H<sub>2</sub>O DW1 amplitude do indeed attain an ~5% error in the zonal-mean component of H<sub>2</sub>O. These aliases further increase the error of the adiabatic displacement method from 8% to almost 13% over the low-latitudes between 65 km and 75 km.

For March equinox, the theoretical approximation of the errors over the low-latitudes reaches no more than 13% while the actual differences between SABER and MLS reach up to 20%. Comparing the zonal-mean component of SABER H<sub>2</sub>O and SD-WACCM-X H<sub>2</sub>O revealed that there are significant differences between them. Between 70 km and 80 km, the SD-WACCM-X H<sub>2</sub>O zonal-mean has lowest values of around 2.5 ppm while SABER's lowest values are only 4

ppm. Also, the gradients above 70 km are larger in SD-WACCM-X than in SABER H<sub>2</sub>O. This indicates that the model may have other errors due to inaccurate photochemistry, residual circulation and gravity wave parameterization. We suggest that this may contribute to the presence of regions with +20% error.

These results therefore lead to the conclusion that the adiabatic displacement method performs best in estimating mesospheric H<sub>2</sub>O DW1 with SABER observations during both March equinox and June solstice over the low latitudes between 65 km and 75 km. Results also show that SD-WACCM-X satisfactorily simulates H<sub>2</sub>O DW1 magnitude and mechanisms only in March equinox. These modeling results show that the errors of the adiabatic displacement method in March equinox may mostly be attributed to aliasing and to the assumption that vertical advection primarily drives H<sub>2</sub>O DW1. It is still unclear why SD-WACCM-X poorly simulates H<sub>2</sub>O DW1 in June solstice but the good agreement between SABER H<sub>2</sub>O advected DW1 and MLS H<sub>2</sub>O DW1 should still support the use of the adiabatic displacement method for this season.

#### **Acknowledgements:**

We would like to acknowledge David E Siskind of the Naval Research Lab for helpful discussions on the SABER H<sub>2</sub>O dataset. This research was supported by grants 109-2636-M-008-004, 110-2636-M-008 -002, 111-2636-M-008 -004, and 110-2923-M-008 -005 -MY3 from the Taiwan Ministry of Science and Technology (Taiwan MOST) to L.C.C., as well as the Higher Education SPROUT grant to the Center for Astronautical Physics and Engineering from the Taiwan Ministry of Education. CCJHS is supported by the aforementioned Taiwan MOST grants and acknowledges high-performance computing support from Cheyenne (doi:10.5065/D6RX99HX) provided by NCAR's Computational and Information Systems Laboratory, sponsored by the National Science Foundation. Q.G. acknowledges the support from the NASA grant (80NSSC20K0721). L.Q. is

supported by grants 80NSSC18K0648, 80NSSC19K0278, 80NSSC20K0189 and  
NNH19ZDA001N-HSR. J.Y., J.R. and M.M. would like to acknowledge the hard work and  
support of the SABER retrieval team who provided the version 2.0 data, including scientists from  
GATS, Inc, NASA Langley Research Center, NASA Goddard Space Flight Center, Spain (IAA),  
and Arcon, Inc. The SABER dataset presented in this paper are accessible from the SABER  
website: <http://saber.gats-inc.com/data.php>. The MLS dataset presented in this paper are accessible  
from the MLS website: <https://aura.gsfc.nasa.gov/mls.html>. As a component of the Community  
Earth System Model, WACCM-X source code and results are publicly available at  
<http://www.cesm.ucar.edu/>.

**References:** Akmaev, R. A., & Shved, G. M. (1980). Modelling of the composition of the lower  
thermosphere taking account of the dynamics with applications to tidal variations of the [OI]  
5577 Å airglow. *Journal of Atmospheric and Terrestrial Physics*, 42(8), 705-716.

Angelats i Coll, M., & Forbes, J. M. (1998). Dynamical influences on atomic oxygen and 5577 Å  
emission rates in the lower thermosphere. *Geophysical research letters*, 25(4), 461-464.

Bernath, P. F., McElroy, C. T., Abrams, M. C., Boone, C. D., Butler, M., Camy-Peyret, C., ... &  
DeCola, P. (2005). Atmospheric chemistry experiment (ACE): mission overview. *Geophysical  
Research Letters*, 32(15).

Brasseur, G. P., & Solomon, S. (2006). *Aeronomy of the middle atmosphere: Chemistry and  
physics of the stratosphere and mesosphere* (Vol. 32). Springer Science & Business Media.

Brewer, A. W. (1949). Evidence for a world circulation provided by the measurements of helium  
and water vapour distribution in the stratosphere. *Quarterly Journal of the Royal Meteorological  
Society*, 75(326), 351-363.



533 Carleer, M. R., Boone, C. D., Walker, K. A., Bernath, P. F., Strong, K., Sica, R. J., ... & Milz, M.  
 534 (2008). Validation of water vapour profiles from the Atmospheric Chemistry Experiment  
 535 (ACE). *Atmospheric Chemistry and Physics Discussions*, 8(2), 4499-4559.

536 Chandra, S., Jackman, C. H., Fleming, E. L., & Russell III, J. M. (1997). The seasonal and long  
 537 term changes in mesospheric water vapor. *Geophysical research letters*, 24(6), 639-642.

538 Chapman, S., & Lindzen, R. S. (1970). Atmospheric tides, 200 pp. *D. Reidel, Norwell, Mass.*

539 Dawkins, E. C. M., Feofilov, A., Rezac, L., Kutepov, A. A., Janches, D., Höffner, J., ... &  
 540 Russell III, J. (2018). Validation of SABER v2. 0 operational temperature data with ground-  
 541 based lidars in the mesosphere-lower thermosphere region (75–105 km). *Journal of Geophysical*  
 542 *Research: Atmospheres*, 123(17), 9916-9934.

543 Dunkerton, T. (1978). On the mean meridional mass motions of the stratosphere and  
 544 mesosphere. *Journal of the Atmospheric Sciences*, 35(12), 2325-2333.

545 Eckermann, S. D., Gibson-Wilde, D. E., & Bacmeister, J. T. (1998). Gravity wave perturbations  
 546 of minor constituents: A parcel advection methodology. *Journal of the atmospheric*  
 547 *sciences*, 55(24), 3521-3539.

548 Engel, A., Bönisch, H., Schwarzenberger, T., Haase, H. P., Grunow, K., Abalichin, J., & Sala, S.  
 549 (2016). Long-term validation of ESA operational retrieval (version 6.0) of MIPAS Envisat  
 550 vertical profiles of methane, nitrous oxide, CFC11, and CFC12 using balloon-borne observations  
 551 and trajectory matching.

552 Forbes, J. M. (1995). Tidal and planetary waves. *The Upper Mesosphere and Lower*  
 553 *Thermosphere: A Review of Experiment and Theory, Geophys. Monogr. Ser.*, 87, 67-87.

554 Gan, Q., Du, J., Ward, W. E., Beagley, S. R., Fomichev, V. I., & Zhang, S. (2014). Climatology  
555 of the diurnal tides from eCMAM30 (1979 to 2010) and its comparison with SABER. *Earth,*  
556 *Planets and Space*, 66(1), 1-24.

557 Garcia, R. R. (1989). Dynamics, radiation, and photochemistry in the mesosphere: Implications  
558 for the formation of noctilucent clouds. *Journal of Geophysical Research:*  
559 *Atmospheres*, 94(D12), 14605-14615.

560 Garcia, R. R., López-Puertas, M., Funke, B., Marsh, D. R., Kinnison, D. E., Smith, A. K., &  
561 González-Galindo, F. (2014). On the distribution of CO<sub>2</sub> and CO in the mesosphere and lower  
562 thermosphere. *Journal of Geophysical Research: Atmospheres*, 119(9), 5700-5718.

563 Garcia, R. R., Smith, A. K., Kinnison, D. E., Cámara, Á. D. L., & Murphy, D. J. (2017).  
564 Modification of the gravity wave parameterization in the Whole Atmosphere Community  
565 Climate Model: Motivation and results. *Journal of the Atmospheric Sciences*, 74(1), 275-291.

566 García-Comas, M., López-Puertas, M., Marshall, B. T., Wintersteiner, P. P., Funke, B., Bermejo-  
567 Pantaleón, D., ... & Russell III, J. M. (2008). Errors in Sounding of the Atmosphere using  
568 Broadband Emission Radiometry (SABER) kinetic temperature caused by non-local-  
569 thermodynamic-equilibrium model parameters. *Journal of Geophysical Research:*  
570 *Atmospheres*, 113(D24).

571 Gordley, L. L., Hervig, M. E., Fish, C., Russell III, J. M., Bailey, S., Cook, J., ... & Marshall, T.  
572 (2009). The solar occultation for ice experiment. *Journal of Atmospheric and Solar-Terrestrial*  
573 *Physics*, 71(3-4), 300-315.

574 Hagan, M. E., & Forbes, J. M. (2002). Migrating and nonmigrating diurnal tides in the middle  
575 and upper atmosphere excited by tropospheric latent heat release. *Journal of Geophysical*  
576 *Research: Atmospheres*, 107(D24).

577 Hagan, M. E., & Forbes, J. M. (2003). Migrating and nonmigrating semidiurnal tides in the  
578 upper atmosphere excited by tropospheric latent heat release. *Journal of Geophysical Research:*  
579 *Space Physics*, 108(A2).

580 Hervig, M., & Siskind, D. (2006). Decadal and inter-hemispheric variability in polar  
581 mesospheric clouds, water vapor, and temperature. *Journal of atmospheric and solar-terrestrial*  
582 *physics*, 68(1), 30-41.

583 Jones, R. L., Pyle, J. A., Harries, J. E., Zavody, A. M., Russell III, J. M., & Gille, J. C. (1986).  
584 The water vapour budget of the stratosphere studied using LIMS and SAMS satellite  
585 data. *Quarterly Journal of the Royal Meteorological Society*, 112(474), 1127-1143.

586 Jones Jr, M., Forbes, J. M., & Hagan, M. E. (2014). Tidal-induced net transport effects on the  
587 oxygen distribution in the thermosphere. *Geophysical Research Letters*, 41(14), 5272-5279.

588 Kunz, A., Pan, L. L., Konopka, P., Kinnison, D. E., & Tilmes, S. (2011). Chemical and  
589 dynamical discontinuity at the extratropical tropopause based on START08 and WACCM  
590 analyses. *Journal of Geophysical Research: Atmospheres*, 116(D24).

591 Lambert, A., Read, W. G., Livesey, N. J., Santee, M. L., Manney, G. L., Froidevaux, L., ... &  
592 Nedoluha, G. E. (2007). Validation of the Aura Microwave Limb Sounder middle atmosphere  
593 water vapor and nitrous oxide measurements. *Journal of Geophysical Research:*  
594 *Atmospheres*, 112(D24).

595 Lee, J. N., Wu, D. L., Manney, G. L., Schwartz, M. J., Lambert, A., Livesey, N. J., ... & Read,  
596 W. G. (2011). Aura Microwave Limb Sounder observations of the polar middle atmosphere:  
597 Dynamics and transport of CO and H<sub>2</sub>O. *Journal of Geophysical Research:*  
598 *Atmospheres*, 116(D5).

599 Liu, A. Z., Lu, X., & Franke, S. J. (2013). Diurnal variation of gravity wave momentum flux and  
600 its forcing on the diurnal tide. *Journal of Geophysical Research: Atmospheres*, 118(4), 1668-  
601 1678.

602 Liu, H. L., Bardeen, C. G., Foster, B. T., Lauritzen, P., Liu, J., Lu, G., ... & Qian, L. (2018).  
603 Development and Validation of the Whole Atmosphere Community Climate Model With  
604 Thermosphere and Ionosphere Extension (WACCM-X 2.0). *Journal of Advances in Modeling*  
605 *Earth Systems*, 10(2), 381-402.

606 Liu, H. L., Hagan, M. E., & Roble, R. G. (2000). Local mean state changes due to gravity wave  
607 breaking modulated by the diurnal tide. *Journal of Geophysical Research:*  
608 *Atmospheres*, 105(D10), 12381-12396.

609 Liu, J., H.-L. Liu, W. Wang, A. G. Burns, Q. Wu, Q. Gan, S. C. Solomon, D. R. Marsh, L. Qian,  
610 G. Lu, N. M. Pedatella, J. M. McInerney, J. M. Russell III, and W. S. Schreiner (2018), First  
611 results from the ionospheric extension of WACCM-X during the deep solar minimum year of  
612 2008, *J. Geophys. Res.*, 123, doi:10.1002/2017JA025010.

613 Manney, G. L., Schwartz, M. J., Krüger, K., Santee, M. L., Pawson, S., Lee, J. N., ... & Livesey,  
614 N. J. (2009). Aura Microwave Limb Sounder observations of dynamics and transport during the  
615 record-breaking 2009 Arctic stratospheric major warming. *Geophysical Research*  
616 *Letters*, 36(12).

617 Marsh, D. R., & Russell III, J. M. (2000). A tidal explanation for the sunrise/sunset anomaly in  
 618 HALOE low-latitude nitric oxide observations. *Geophysical research letters*, 27(19), 3197-3200.

619 Marsh, D. R., Mills, M. J., Kinnison, D. E., Lamarque, J. F., Calvo, N., & Polvani, L. M. (2013).  
 620 Climate change from 1850 to 2005 simulated in CESM1 (WACCM). *Journal of climate*, 26(19),  
 621 7372-7391.

622 Marsh, D. R., Skinner, W. R., & Yudin, V. A. (1999). Tidal influences on O<sub>2</sub> atmospheric band  
 623 dayglow: HRDI observations vs. model simulations. *Geophysical research letters*, 26(10), 1369-  
 624 1372.

625 McLandress, C. (1997). Seasonal variability of the diurnal tide: Results from the Canadian  
 626 middle atmosphere general circulation model. *Journal of Geophysical Research:*  
 627 *Atmospheres*, 102(D25), 29747-29764.

628 Mertens, C. J., Russell III, J. M., Mlynczak, M. G., She, C. Y., Schmidlin, F. J., Goldberg, R.  
 629 A., ... & Xu, X. (2009). Kinetic temperature and carbon dioxide from broadband infrared limb  
 630 emission measurements taken from the TIMED/SABER instrument. *Advances in Space*  
 631 *Research*, 43(1), 15-27.

632 Mukhtarov, P., Pancheva, D., & Andonov, B. (2009). Global structure and seasonal and  
 633 interannual variability of the migrating diurnal tide seen in the SABER/TIMED temperatures  
 634 between 20 and 120 km. *Journal of Geophysical Research: Space Physics*, 114(A2).

635 Nedoluha, G. E., Bevilacqua, R. M., Gomez, R. M., Waltman, W. B., Hicks, B. C., Thacker, D.  
 636 L., & Matthews, W. A. (1996). Measurements of water vapor in the middle atmosphere and  
 637 implications for mesospheric transport. *Journal of Geophysical Research:*  
 638 *Atmospheres*, 101(D16), 21183-21193.

639 Oberheide, J., & Forbes, J. M. (2008). Thermospheric nitric oxide variability induced by  
 640 nonmigrating tides. *Geophysical Research Letters*, 35(16).

641 Oberheide, J., Hagan, M. E., & Roble, R. G. (2003). Tidal signatures and aliasing in temperature  
 642 data from slowly precessing satellites. *Journal of Geophysical Research: Space Physics*,  
 643 108(A2).

644 Orsolini, Y. J., Urban, J., Murtagh, D. P., Lossow, S., & Limpasuvan, V. (2010). Descent from  
 645 the polar mesosphere and anomalously high stratopause observed in 8 years of water vapor and  
 646 temperature satellite observations by the Odin Sub-Millimeter Radiometer. *Journal of*  
 647 *Geophysical Research: Atmospheres*, 115(D12).

648 Pancheva, D., Mukhtarov, P., & Andonov, B. (2009, February). Global structure, seasonal and  
 649 interannual variability of the migrating semidiurnal tide seen in the SABER/TIMED  
 650 temperatures (2002-2007). In *Annales geophysicae: atmospheres, hydrospheres and space*  
 651 *sciences* (Vol. 27, No. 2, p. 687).

652 Raspollini, P., Belotti, C., Burgess, A., Carli, B., Carlotti, M., Ceccherini, S., ... & Höpfner, M.  
 653 (2006). MIPAS level 2 operational analysis.

654 Remsberg, E. E., Marshall, B. T., Garcia-Comas, M., Krueger, D., Lingenfelser, G. S., Martin-  
 655 Torres, J., ... & Brown, C. (2008). Assessment of the quality of the Version 1.07 temperature-  
 656 versus-pressure profiles of the middle atmosphere from TIMED/SABER. *Journal of Geophysical*  
 657 *Research: Atmospheres*, 113(D17).

658 Remsberg, E., Damadeo, R., Natarajan, M., & Bhatt, P. (2018). Observed responses of  
 659 mesospheric water vapor to solar cycle and dynamical forcings. *Journal of Geophysical*  
 660 *Research: Atmospheres*, 123(7), 3830-3843.

661 Rezac, L., Kutepov, A., Russell III, J. M., Feofilov, A. G., Yue, J., & Goldberg, R. A. (2015).  
 662 Simultaneous retrieval of T (p) and CO<sub>2</sub> VMR from two-channel non-LTE limb radiances and  
 663 application to daytime SABER/TIMED measurements. *Journal of Atmospheric and Solar-*  
 664 *Terrestrial Physics*, 130, 23-42.

665 Richter, J. H., Sassi, F., & Garcia, R. R. (2010). Toward a physically based gravity wave source  
 666 parameterization in a general circulation model. *Journal of the Atmospheric Sciences*, 67(1),  
 667 136-156.

668 Rienecker, M. M., Suarez, M. J., Gelaro, R., Todling, R., Bacmeister, J., Liu, E., ... & Woollen,  
 669 J. (2011). MERRA: NASA's modern-era retrospective analysis for research and  
 670 applications. *Journal of climate*, 24(14), 3624-3648.

671 Rong, P., Russell III, J. M., Marshall, B. T., Gordley, L. L., Mlynczak, M. G., & Walker, K. A.  
 672 (2019). Validation of water vapor measured by SABER on the TIMED satellite. *Journal of*  
 673 *Atmospheric and Solar-Terrestrial Physics*, 194, 105099.

674 Russell, J. M., III, M. G. Mlynczak, L. L. Gordley, J. J. Tansock Jr., and R. W. Esplin (1999),  
 675 Overview of the SABER experiment and preliminary calibration results, SPIE Proc., 3756, 277–  
 676 288, doi:10.1117/12.366382.

677 Salinas, C. C. J. H., Chang, L. C., Liang, M. C., Yue, J., Qian, L., Gan, Q., ... & Mlynczak, M.  
 678 (2020). Local-Time Variabilities of March Equinox Daytime SABER CO<sub>2</sub> in the Upper  
 679 Mesosphere and Lower Thermosphere Region. *Journal of Geophysical Research: Space*  
 680 *Physics*, 125(3), e2019JA027039.

681 Shepherd, G. G., McLandress, C., & Solheim, B. H. (1995). Tidal influence on O (<sup>1</sup>S) Airglow  
682 emission rate distributions at the geographic equator as observed by WINDII. *Geophysical*  
683 *Research Letters*, 22(3), 275-278.

684 Shepherd, G. G., Roble, R. G., McLandress, C., & Ward, W. E. (1997). WINDII observations of  
685 the 558 nm emission in the lower thermosphere: the influence of dynamics on  
686 composition. *Journal of Atmospheric and Solar-Terrestrial Physics*, 59(6), 655-667.

687 Smith, A. K., & Brasseur, G. P. (1991). Numerical simulation of the seasonal variation of  
688 mesospheric water vapor. *Journal of Geophysical Research: Atmospheres*, 96(D4), 7553-7563.

689 Smith, A. K., Garcia, R. R., Marsh, D. R., & Richter, J. H. (2011a). WACCM simulations of the  
690 mean circulation and trace species transport in the winter mesosphere. *Journal of Geophysical*  
691 *Research: Atmospheres*, 116(D20).

692 Smith, A. K., Harvey, V. L., Mlynczak, M. G., Funke, B., García-Comas, M., Hervig, M., ... &  
693 Walker, K. A. (2013). Satellite observations of ozone in the upper mesosphere. *Journal of*  
694 *Geophysical Research: Atmospheres*, 118(11), 5803-5821.

695 Smith, A. K., Marsh, D. R., Mlynczak, M. G., & Mast, J. C. (2010). Temporal variations of  
696 atomic oxygen in the upper mesosphere from SABER. *Journal of Geophysical Research:*  
697 *Atmospheres*, 115(D18).

698 Smith, A. K., Marsh, D. R., Mlynczak, M. G., Russell, J. M., & Mast, J. C. (2011b). SABER  
699 observations of daytime atomic oxygen and ozone variability in the mesosphere. In *Aeronomy of*  
700 *the Earth's Atmosphere and Ionosphere* (pp. 75-82). Springer, Dordrecht.



701 Summers, M. E., Siskind, D. E., Bacmeister, J. T., Conway, R. R., Zasadil, S. E., & Strobel, D.  
702 F. (1997). Seasonal variation of middle atmospheric CH<sub>4</sub> and H<sub>2</sub>O with a new chemical-  
703 dynamical model. *Journal of Geophysical Research: Atmospheres*, 102(D3), 3503-3526.

704 Walterscheid, R. L. (1981). Dynamical cooling induced by dissipating internal gravity  
705 waves. *Geophysical Research Letters*, 8(12), 1235-1238.

706 Ward, W. E. (1998). Tidal mechanisms of dynamical influence on oxygen recombination airglow  
707 in the mesosphere and lower thermosphere. *Advances in Space Research*, 21(6), 795-805.

708 Ward, W. E. (1999). A simple model of diurnal variations in the mesospheric oxygen  
709 nightglow. *Geophysical research letters*, 26(23), 3565-3568.

710 Waters, J. W., Froidevaux, L., Harwood, R. S., Jarnot, R. F., Pickett, H. M., Read, W. G., ... &  
711 Holden, J. R. (2006). The earth observing system microwave limb sounder (EOS MLS) on the  
712 Aura satellite. *IEEE Transactions on Geoscience and Remote Sensing*, 44(5), 1075-1092.

713 Wetzel, G., Oelhaf, H., Berthet, G., Bracher, A., Cornacchia, C., Feist, D. G., ... & Lengel, A.  
714 (2013). Validation of MIPAS-ENVISAT H<sub>2</sub>O operational data collected between July 2002 and  
715 March 2004. *Atmospheric Chemistry and Physics*, 13, 5791-5811.

716 Wu, D. L., Hays, P. B., & Skinner, W. R. (1995). A least squares method for spectral analysis of  
717 space-time series. *Journal of Atmospheric Sciences*, 52(20), 3501-3511.

718 Yu, W., Garcia, R., Yue, J., Russell III, J., & Mlynczak, M. Variability of water vapor in the  
719 tropical middle atmosphere observed from satellites and interpreted using SD-WACCM  
720 simulations. *Journal of Geophysical Research: Atmospheres*, e2022JD036714.

721 Yue, J. and Gan, Q., Quasi-two-day wave modulation of carbon dioxide in the mesosphere and  
722 lower thermosphere, *Journal of Atmospheric and Solar-Terrestrial Physics* (2021),  
723 doi:<https://doi.org/10.1016/j.jastp.2021.105750>.

724 Yue, J., Russell III, J., Gan, Q., Wang, T., Rong, P., Garcia, R., & Mlynarczyk, M. (2019).  
725 Increasing water vapor in the stratosphere and mesosphere after 2002. *Geophysical Research*  
726 *Letters*, 46(22), 13452-13460.

727 Zhang, S. P., Wiens, R. H., Solheim, B. H., & Shepherd, G. G. (1998). Nightglow zenith  
728 emission rate variations in O (1 S) at low latitudes from wind imaging interferometer (WINDII)  
729 observations. *Journal of Geophysical Research: Atmospheres*, 103(D6), 6251-6259.

730 Zhang, X., Forbes, J. M., Hagan, M. E., Russell, J. M., Palo, S. E., Mertens, C. J., & Mlynarczyk,  
731 M. G. (2006). Monthly tidal temperatures 20–120 km from TIMED/SABER. *Journal of*  
732 *Geophysical Research: Space Physics*, 111(A10).

733

734 Figure 1: (1.A) March equinox latitude-altitude profile of the DW1 amplitudes of SABER H<sub>2</sub>O.  
735 (1.B) March equinox latitude-altitude profile of the DW1 phases of SABER H<sub>2</sub>O. (1.C) March  
736 equinox latitude-altitude profile of the DW1 amplitudes of SD-WACCM-X H<sub>2</sub>O. (1.D) March  
737 equinox latitude-altitude profile of the DW1 phases of SD-WACCM-X H<sub>2</sub>O. Units are specified  
738 in the plots. (1.E) Alias on the zonal-mean DW1 due to SABER H<sub>2</sub>O DW1.

739

740 Figure 2: (2.A) Zonal-mean component of SABER H<sub>2</sub>O for March equinox. (2.B) Vertical gradient  
741 of the zonal-mean component of SABER H<sub>2</sub>O for March equinox. (2.C) March equinox latitude-

altitude profile of the DW1 amplitudes of SABER temperatures. (2.D) March equinox latitude-altitude profile of the SABER advected H<sub>2</sub>O DW1 amplitudes. (2.E) Difference between SABER H<sub>2</sub>O reconstructed at 2AM and at 2PM in March equinox as a function of latitude and altitude. (2.F) Difference between MLS H<sub>2</sub>O at 2AM and at 2PM in March equinox as a function of latitude and altitude. Units are specified in the plots.

Figure 3: Same as figure 2 but for June solstice.

Figure 4: (4.A) Zonal-mean component of SD-WACCM-X H<sub>2</sub>O for March equinox. (4.B) Vertical gradient of the zonal-mean component of SD-WACCM-X H<sub>2</sub>O for March equinox. (4.C) March equinox latitude-altitude profile of the DW1 amplitudes of SD-WACCM-X temperatures. (4.D) March equinox latitude-altitude profile of the SD-WACCM-X advected H<sub>2</sub>O DW1 amplitudes. (4.E) Percent difference in March equinox between SD-WACCM-X advected H<sub>2</sub>O DW1 amplitudes and SD-WACCM-X H<sub>2</sub>O DW1 amplitudes. Units are specified in the plots.

Figure 5: (5.A) Zonal-mean component of SD-WACCM-X H<sub>2</sub>O for June solstice. (5.B) Vertical gradient of the zonal-mean component of SD-WACCM-X H<sub>2</sub>O for June solstice. (5.C) June solstice latitude-altitude profile of the DW1 amplitudes of SD-WACCM-X temperatures. (5.D) June solstice latitude-altitude profile of the DW1 amplitudes of SD-WACCM-X H<sub>2</sub>O. (5.E) June solstice latitude-altitude profile of the SD-WACCM-X advected H<sub>2</sub>O DW1 amplitudes. (5.F) Percent difference in June solstice between SD-WACCM-X advected H<sub>2</sub>O DW1 amplitudes and SD-WACCM-X H<sub>2</sub>O DW1 amplitudes. Units are specified in the plots.

764

765 Figure 6: March equinox latitude-altitude profile of the DW1 amplitudes of (6.A)  $\left(\frac{\partial}{\partial t} + \frac{\bar{u}}{a \cos \phi}\right) \mu'$ ,  
766 (6.B) vertical advection, (6.C) meridional advection, (6.D) chemical loss tendency, (6.E) eddy  
767 diffusion and (6.F) molecular diffusion. Units are all in ppm/day.

768

769 Figure 7: Same as figure 6 but for June solstice.

770

771 Figure 8: (8.A) SD-WACCM-X H<sub>2</sub>O zonal-mean with alias. (8.B) Percent error on SD-WACCM-  
772 X H<sub>2</sub>O zonal-mean due to alias. (8.C) March equinox latitude-altitude profile of the SD-WACCM-  
773 X advected H<sub>2</sub>O DW1 amplitudes constructed with a zonal-mean profile containing alias. (8.D)  
774 Percent error between SD-WACCM-X advected H<sub>2</sub>O DW1 amplitudes with aliasing and SD-  
775 WACCM-X H<sub>2</sub>O DW1 amplitudes. Units are specified in the plots.

776

777

778

779

780

781

782

783

784

785

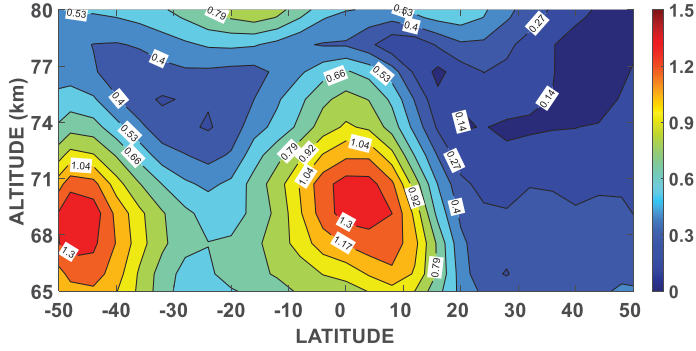
786

787

Figure 1.

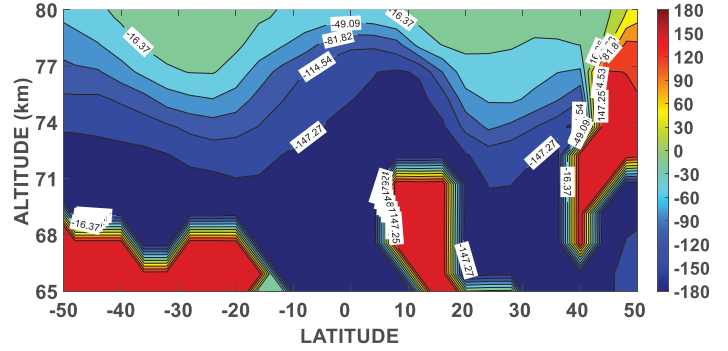
(A)

MEQX SABER H2O DW1 AMP (ppm)



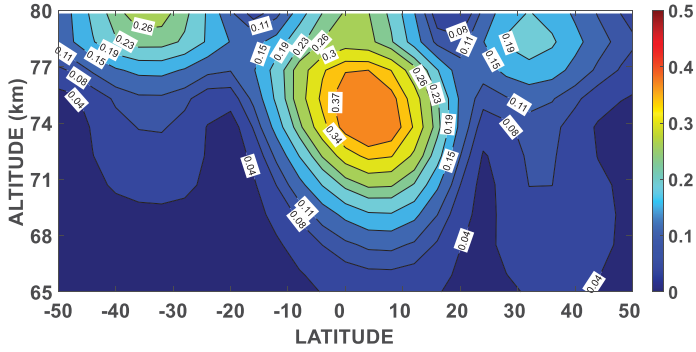
(B)

MEQX SABER H2O DW1 PH (deg)



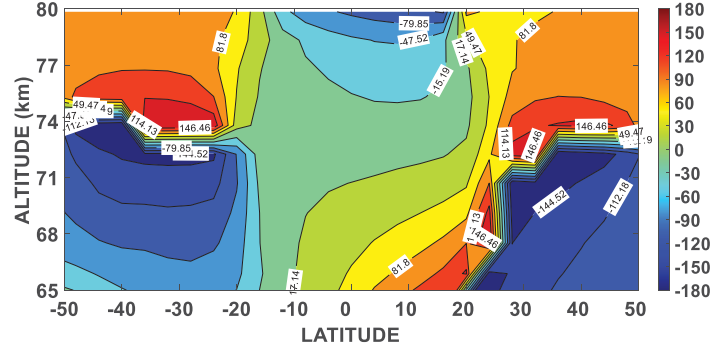
(C)

MEQX SD-WACCM-X DW1 AMP H2O (ppm)



(D)

MEQX SD-WACCM-X DW1 PH H2O (deg)



(E)

ZONAL-MEAN ALIAS DUE TO DW1 (ppm)

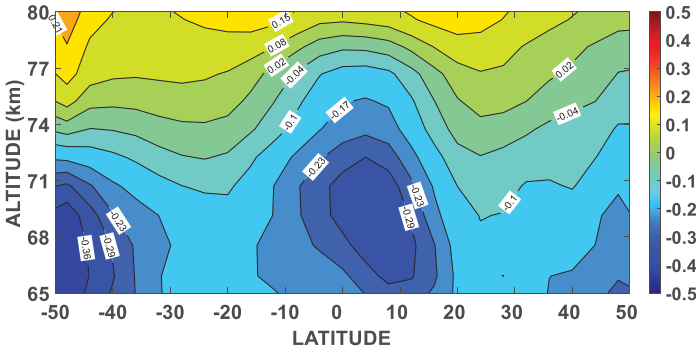


Figure 2.





Figure 3.

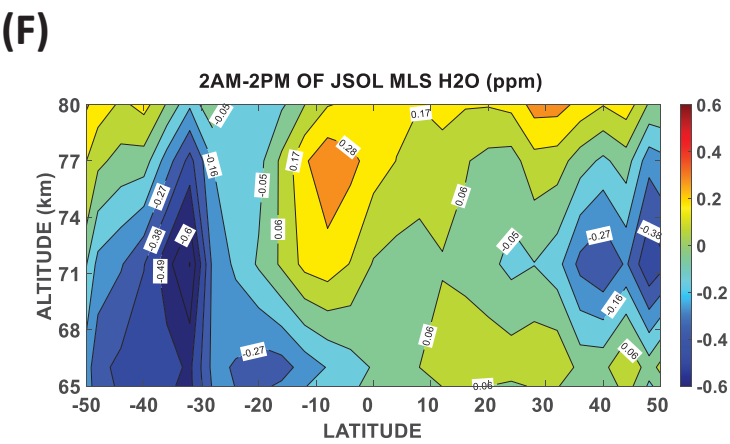
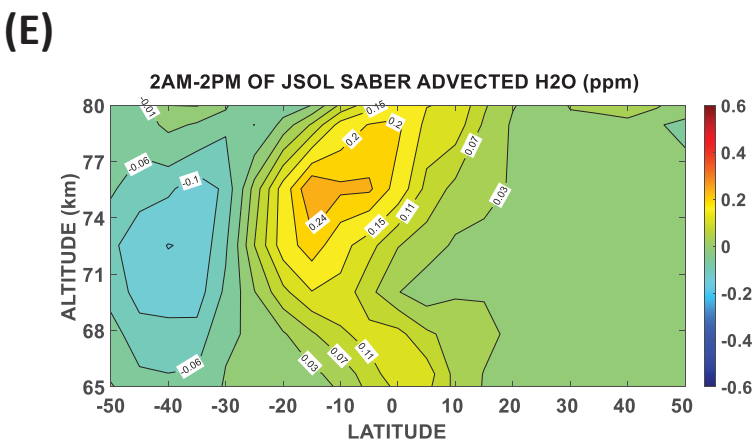
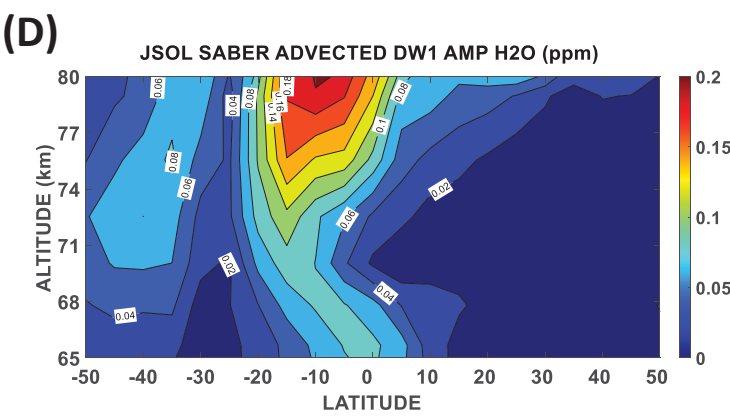
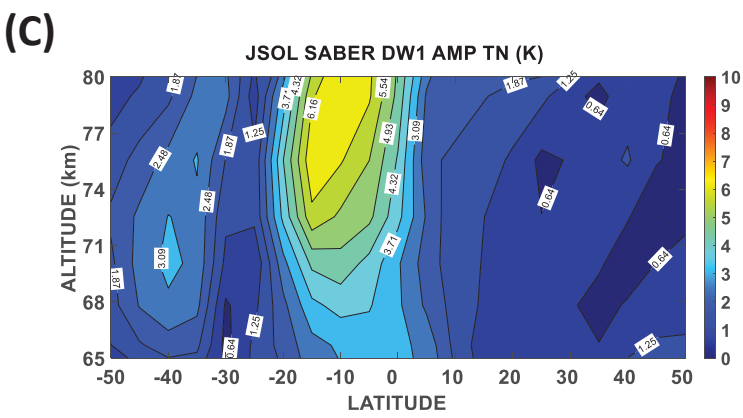
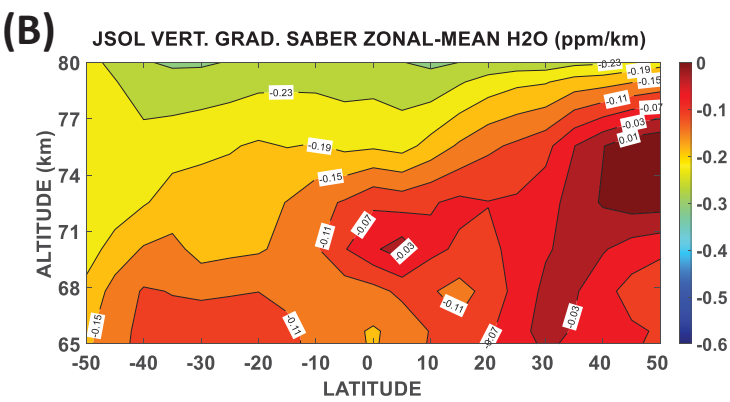
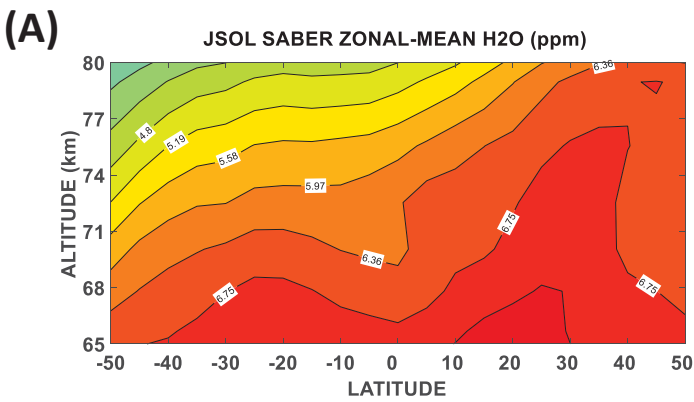


Figure 4.

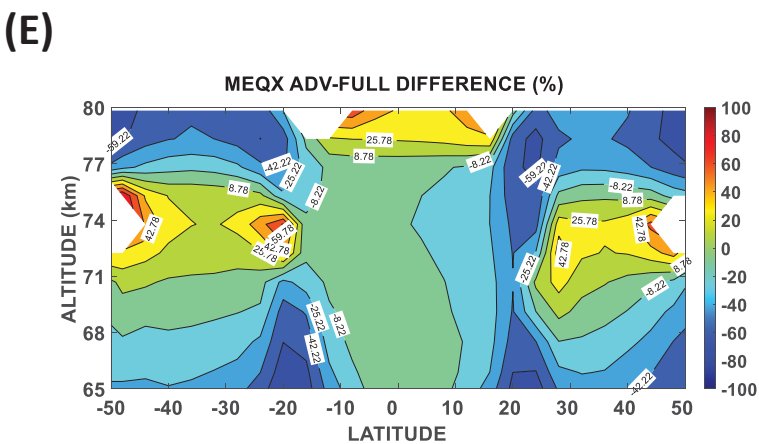
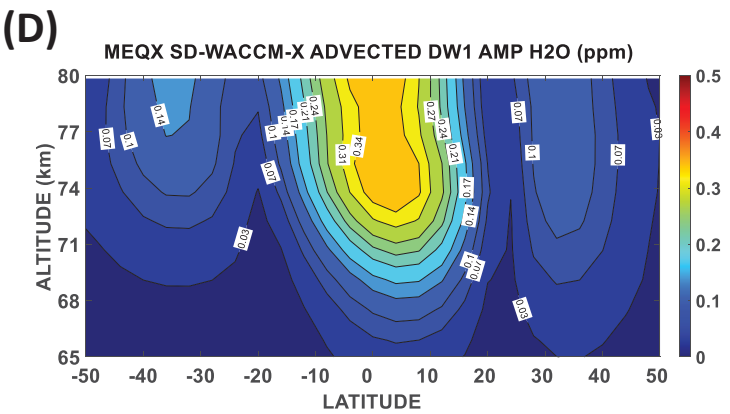
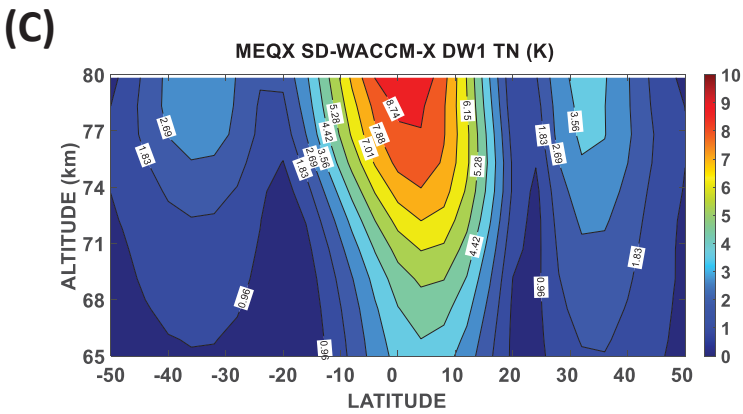
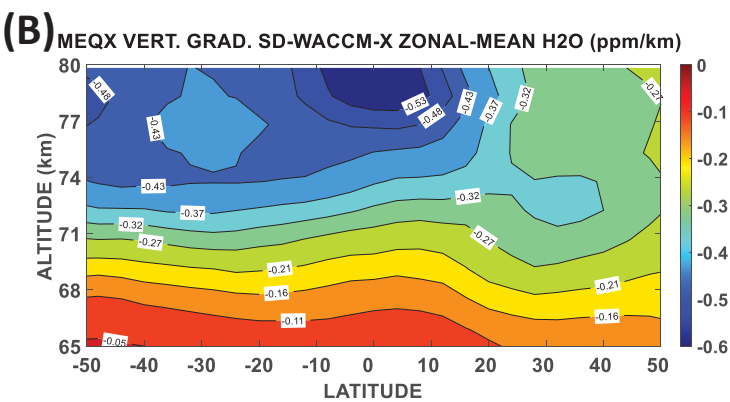
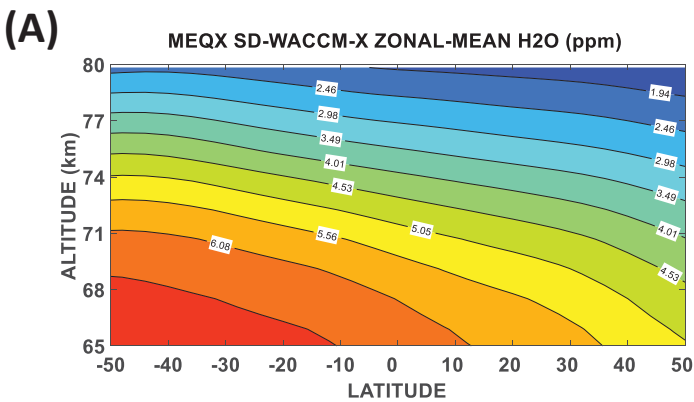


Figure 5.

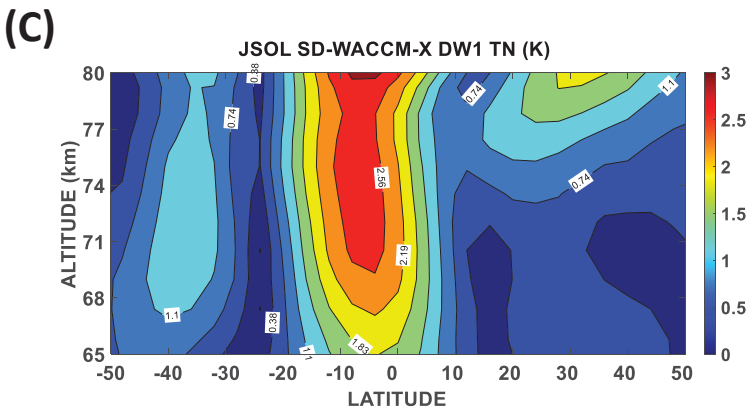
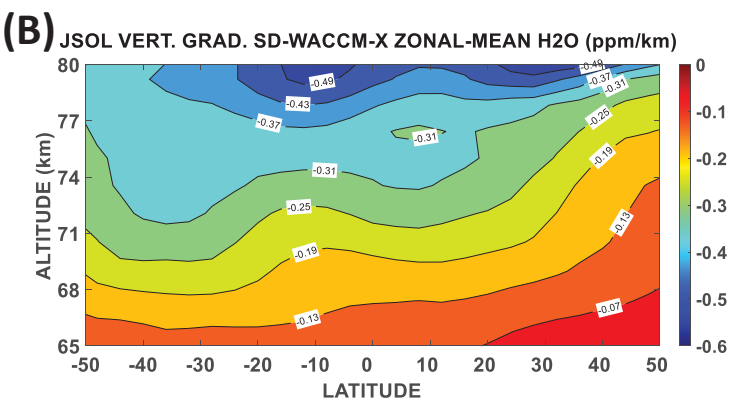
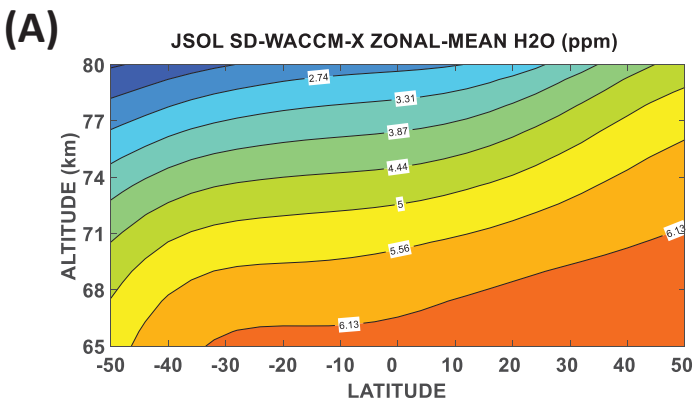


Figure 6.



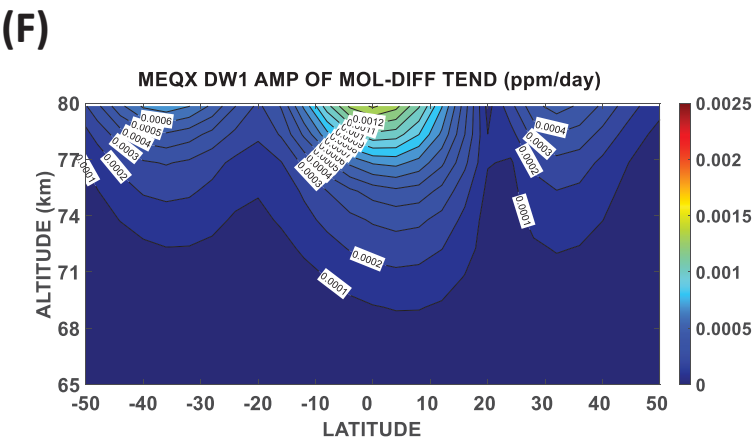
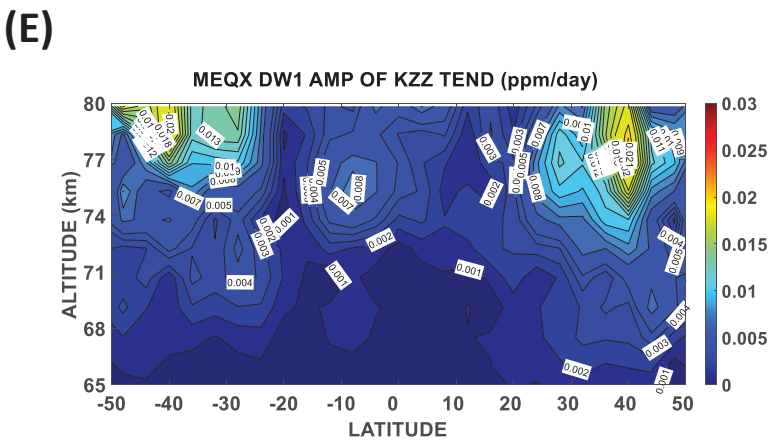
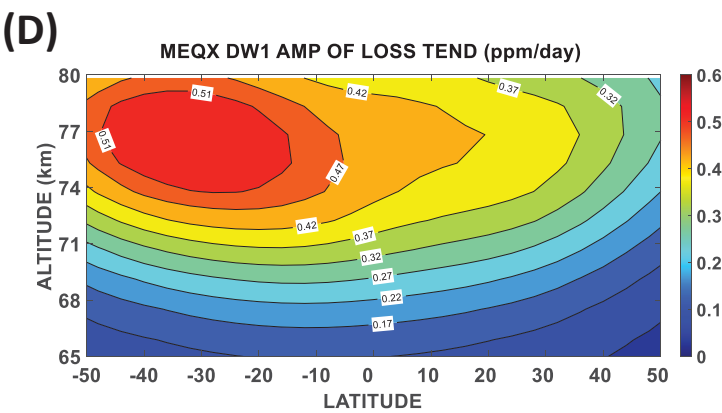
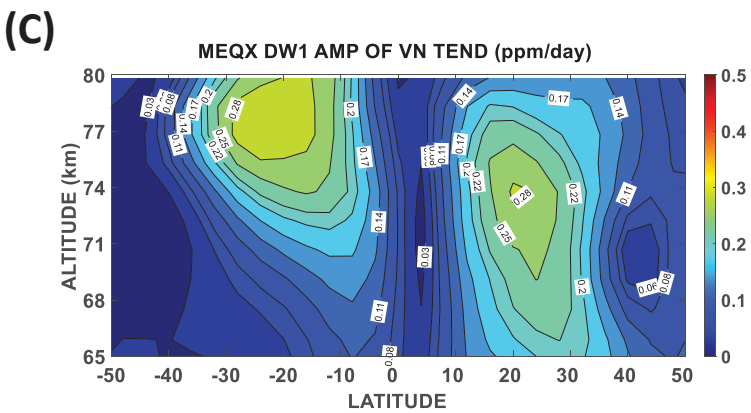
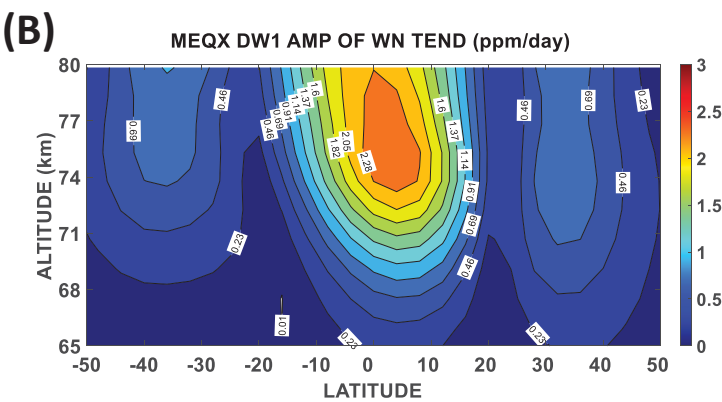
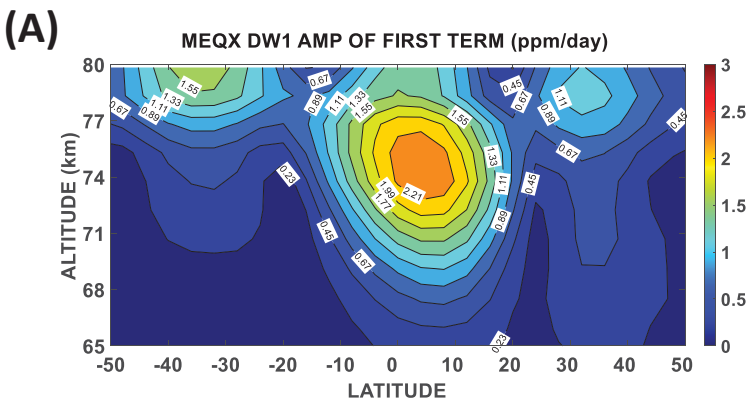
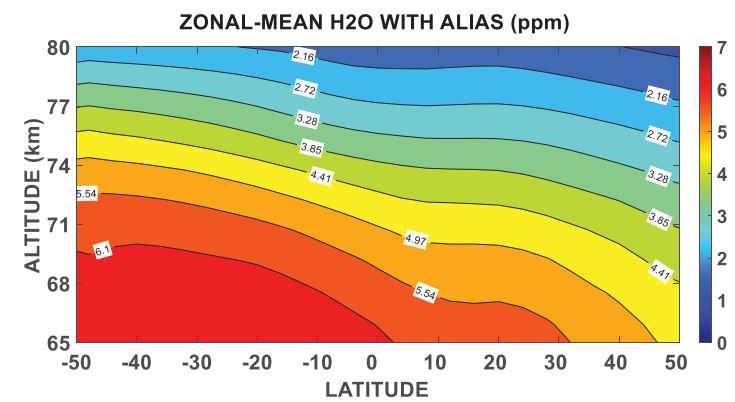


Figure 7.

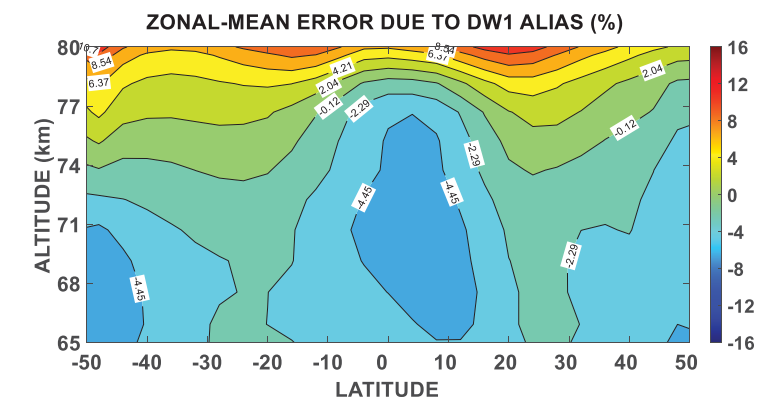


Figure 8.

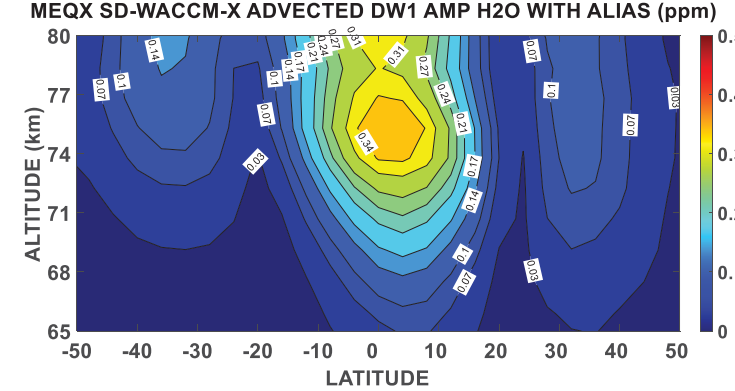
(A)



(B)



(C)



(D)

